Material Design and Optimisation of Electrochemical Li-Ion Storage Properties of Ternary Silicon Oxycarbide/Graphite/Tin Nanocomposites

Dominik Knozowski [1], **Pradeep Vallachira Warriam Sasikumar** [2], **Piotr Madajski** [3], **Gurdial Blugan** [2], **Maria Gazda** [4], **Natalia Kovalska** [2] **and Monika Wilamowska-Zawłocka** [1,*]

1   Department of Energy Conversion and Storage, Faculty of Chemistry, Gdańsk University of Technology, Narutowicza 11/12, 80-233 Gdańsk, Poland; dominik.knozowski@pg.edu.pl
2   Laboratory for High Performance Ceramics, Empa, Swiss Federal Laboratories for Materials Science & Technology, CH-8600 Dübendorf, Switzerland; pradeep.variyar@gmail.com (P.V.W.S.); Gurdial.Blugan@empa.ch (G.B.); natalia.kovalska@empa.ch (N.K.)
3   Faculty of Chemistry, Nicolaus Copernicus University in Torun, 87-100 Toruń, Poland; piotr.madajski@doktorant.umk.pl
4   Department of Solid State Physics, Faculty of Applied Physics and Mathematics, Gdańsk University of Technology, Narutowicza 11/12, 80-233 Gdańsk, Poland; margazda@pg.edu.pl
*   Correspondence: monika.wilamowska@pg.edu.pl

Abstract: In this work, we present the characterization and electrochemical performance of various ternary silicon oxycarbide/graphite/tin (SiOC/C/Sn) nanocomposites as anodes for lithium-ion batteries. In binary SiOC/Sn composites, tin nanoparticles may be produced in situ via carbothermal reduction of SnO_2 to metallic Sn, which consumes free carbon from the SiOC ceramic phase, thereby limiting the carbon content in the final ceramic nanocomposite. Therefore, to avoid drawbacks with carbon depletion, we used graphite as a substitute during the synthesis of precursors. The ternary composites were synthesized from liquid precursors and flake graphite using the ultrasound-assisted hydrosilylation method and pyrolysis at 1000 °C in an Ar atmosphere. The role of the graphitic component is to ensure good electric conductivity and the softness of the material, which are crucial for long term stability during alloying–dealloying processes. The presented approach allows us to increase the content of the tin precursor from 40 wt.% to 60 wt.% without losing the electrochemical stability of the final material. The charge/discharge capacity (at 372 mA g^{-1} current rate) of the tailored SiOC/C/Sn composite is about 100 mAh g^{-1} higher compared with that of the binary SiOC/Sn composite. The ternary composites, however, are more sensitive to high current rates (above 372 mA g^{-1}) compared to the binary one because of the presence of graphitic carbon.

Keywords: silicon oxycarbide; tin nanoparticles; Li-ion battery; ternary composites; graphite

1. Introduction

The exceptional storage capabilities of tin, such as the high gravimetric capacity of 994 mAh g^{-1} and the relatively low lithiation potential of 0.6 V [1–3], make it an appealing anodic material for lithium-ion batteries. Indeed, much effort has been devoted to developing stable tin-based anodes. The number one obstacle to overcome is their high-volume expansion of around 260% during the lithium insertion process. This leads to pulverization of electrodes, i.e., material rupture and disintegration upon cyclic volume changes, resulting in poor electrochemical stability over continuous charge/discharge cycles [4]. The most common way to prevent pulverization is the reduction of Sn particle size to the nanometre scale [5,6] and their homogenous distribution in a matrix to prevent their agglomeration. Moreover, the matrix has to be able to withstand the strain created upon volume expansion during cycling. Multiple materials have been tested as a potential matrix for Sn nanoparticles (NPs), including metal-based [7,8], carbon-based [9,10], and

ceramic-based materials [11–14]. From these three types of matrices, polymer-derived ceramics (PDCs) deserve special attention because of their useful and unique features. From the PDC family, silicon oxycarbides (SiOCs) have been widely studied as anodes for Li-ion batteries, as they exhibit a high capacity of ~600 mAh g^{-1}, good stability, and high rate capability [15,16]. SiOCs are produced by pyrolysis of preceramic precursors, such as polysiloxanes, polysilsesquioxanes, and polycarbosiloxanes [17]. They are amorphous structures consisting of short-range ordered silicon–oxygen–carbon tetrahedra (SiO$_x$C$_{4-x}$, x = 0–4) surrounded by a free carbon phase. Their composition and structure can be easily tailored through multiple synthesis routes [18–25]. Moreover, SiOCs exhibit good mechanical properties and low volume expansion upon lithiation, which makes them great candidates for electrochemically active matrices for Li-alloying nanoparticles. It has been shown that a large amount of free carbon phase dispersed in the ceramic matrix stabilizes nanoparticles over extended charge–discharge cycles [11].

One of the ways to incorporate Sn NPs into the ceramic matrix is by mixing a preceramic polymer with a liquid tin precursor in the pre-pyrolysis stage. To obtain a homogenous mixture, assuring the uniform dispersion of Sn particles in the matrix as well as their nanometre size, the polarity of a tin precursor has to match the polarity of the preceramic polymer [13]. The formation of tin nanoparticles takes place upon pyrolysis in a two-step process. Firstly, tin oxide is formed at low temperatures (>200 degrees), followed by their carbothermal reduction into metallic tin (>700 degrees), consuming the carbon present in the ceramic matrix. This process leads to uniformly distributed Sn NPs, but at the same time, it also reduces the carbon content in the final material. The carbon phase in SiOC-based composites is essential for ensuring the appropriate softness of the material and electrical conductivity [12,15,26]. Insufficient carbon content within the material causes quick performance fading, and for the best performing material, the tin content within the ceramic matrix is limited to a maximum of ~30 wt.% [13].

The addition of an extra source of carbon during preceramic synthesis is expected to be beneficial for increasing the tin content in the final ceramic nanocomposites. The carbon content in SiOCs may be increased by admixing heavy aromatic hydrocarbons, such as pitch [27,28], divinylbenzene (DVB) [29,30], and polystyrene [31], or by adding carbonaceous materials, such as graphene [32,33], carbon nanotubes [34], and graphite [35–38]. The incorporation of graphite is an interesting option for a couple of reasons. Graphite is a very cheap, abundant, and non-toxic material. Moreover, it exhibits a stable electrochemical response and low-volume expansion upon lithium insertion, and it has one of the lowest lithiation potentials of 0.05 V [3]. Graphite was already successfully applied in combination with PDCs [35,37–39]. It is worth noting that the addition of graphite to the ceramic material may induce different electrochemical properties, depending on the composition of the preceramic polymer and the polymer-to-graphite ratio [35]. A capacity increase, a lower lithiation potential, a higher first-cycle Coulombic efficiency, and a better rate capability were observed for various SiOC/graphite composites, which have been mostly attributed to the improved conductivity, the creation of new lithium storage sites [37,38], and the appropriate ratio between ordered (graphitic) and disordered carbons [35]. Graphite was also reported to be a good component for Sn-based nanocomposites due to its low volume expansion and good electrical conductivity [5]. Graphite reduces charge transfer resistance and lowers overall polarization [40]. In addition, the graphite/tin composite exhibits a remarkably improved capacity at low temperatures in comparison with pure graphitic anodes [41].

In this work, we combined graphite and SiOC to achieve an exceptional matrix for tin nanoparticles and increase carbon content, which is a crucial component for ensuring good conductivity. The idea behind the addition of graphite was also to increase the tin content in the final material compared with that of the pure carbon-rich ceramic matrix. The ternary silicon oxycarbide/graphite/tin composites were synthesised using a poly(methylhydrosiloxane)–divinylbenzene mixture as a preceramic precursor, tin (II) octoate as a tin source, and graphite flakes. The choice of the preceramic polymer

and the tin source was based on the good miscibility of these components as reported by Dubey et al. [13]. The main focus of this work was on the influence of graphite with regard to the progress of carbothermal reduction processes as well as the composition, microstructure, and electrochemical behaviour of the final composites.

2. Materials and Methods

Synthesis of SiOC/C/Sn Composites

Starting materials: Polymethylhydrosiloxane (PMHS, MW $\approx$ 1900), divinylbenzene (DVB, technical grade, 80%), graphite (flakes, 20 μm), tin octoate (Sn(Oct)$_2$, 92.5–100.0%, Sigma-Aldrich), Karstedt's catalyst (2% of Pt element in xylene), and acetone ($\geq$99.5%) were purchased from Sigma Aldrich, Buchs, Switzerland. All materials were used as received.

Synthesis of the active materials: The composites were synthesised using the ultrasound-enhanced hydrosilylation method. First, 5 μL of Karstedt's catalyst was added to 2 g of DVB. Then, after 2 min of intense stirring, 2 g of PMHS, 2.5 g of acetone, and different amounts of graphite and tin octoate were added to the mixture. After a couple of minutes of stirring, the suspension was treated with an ultrasonic probe sonicator for 3–5 min to obtain a solid gel. The gels of various compositions were dried for two days at 80 °C to complete crosslinking. Finally, the green bodies were pyrolyzed using the following programme: heating to 250 °C with a rate of 100 °C h^{-1}, dwelling at 250 °C for 2 h, heating to 1000 °C with a rate of 150 °C h^{-1}, dwelling at 1000 °C for 1 h, cooling to room temperature with a rate of 60 °C h^{-1}. The compositions of the preceramic blends are presented in Table 1. The matrix was composed either of the pure ceramic (SiOC) or the ceramic mixed with graphite (SiOC:C$_x$, where the "x" value corresponds to the mass fraction of graphite replacing the preceramic polymer). The tin precursor content is denoted as Sn-y%, where "y" corresponds to the weight percentage of the tin precursor with regard to the mass of the whole preceramic polymeric blend.

Table 1. Compositions of the preceramic blends.

Composite	Tin Octoate	Matrix	
		Graphite	PMHS/DVB; 1:1 w/w Ratio
SiOC	-	-	5 g
SiOC/Sn-40%	3.33 g	-	5 g
SiOC:C$_{0.2}$/Sn-40%	3.33 g	1 g	4 g
SiOC:C$_{0.2}$/Sn-60%	7.5 g	1 g	4 g
SiOC:C$_{0.1}$/Sn-60%	7.5 g	0.5 g	4.5 g

Characterization techniques: Raman analysis was conducted using a micro-Raman spectrometer (InVia, Renishaw, Wotton-under-Edge, UK) equipped with an Ar ion laser (514 nm) within 100–3200 cm^{-1}. The analysis of obtained spectra was performed using OriginPro2016 software after background subtraction with custom settings. The modes were fitted according to [42], using Lorentzian fitting for D4, D1, G, and D2 peaks, and Gaussian fitting for the D3 peak. XRD reflexes were collected using the EDAX, RTEM model SN9577. The morphology of obtained materials was characterised using a scanning electron microscope (Tescan VEGA, Tescan, Brno, Czech Republic) and a transmission electron microscope (FEI, G2 F20X-Twin 200 kV, FEG), while the surface elemental distribution was assessed using a Phenom XL Scanning Electron Microscope (ThermoFisher Scientific, Warsaw, Poland) equipped with an energy dispersive X-ray (EDX) microanalyser. Brunauer–Emmett–Teller (BET) surface area analysis was performed on a BET analyser (SA 3100, Beckman Coulter, Brea, California, USA). Magic angle spinning nuclear magnetic resonance (MAS NMR) measurements for silicon ^{29}Si NMR were conducted on the Bruker Avance Ultrashield 500 MHz spectrometer (Billerica, MA, U.S) and the Avance Ultrashield 500 MHz spectrometer (Waltham, MA, USA). The parameters were as follows: single pulse sequence, ^{29}Si frequency: 139.11 MHz, π/8 pulse length: 2.5 ms, recycle delay: 100 s, 1 k scans, external secondary reference: DSS. Under air flow, 3.2 mm zirconia rotors filled with samples were

spun at 8 kHz. The spectra were fitted using OriginPro2016 software, assuming they consisted of Lorenz type peak components.

Electrochemical measurements: Electrodes for electrochemical testing were prepared using the doctor blade technique. First, the finely grounded active material (85 wt.%) was ball milled with carbon black (7.5 wt.%, Super P, TIMCAL, Bodio, Switzerland) at 350 rpm. Then, carboxymethyl cellulose (7.5 wt.%, CMC, SUNROSE MAC 500LC, Nippon Paper Group) solution in water was added to the active material/carbon black mixture, and then all components were further ball milled for 1.5 h. The obtained slurries were coated on Cu foil, and the layers were then dried overnight in a vacuum oven at 120 °C. Swagelok® type cells were prepared using 1 M $LiPF_6$ in EC:DMC (1:1) (ethylene carbonate: dimethyl carbonate, BASF, battery grade, >98%, TCI Chemicals (Portland, OR, USA), a soaked glass microfiber separator (MN GF-2, Macherey-Nagel GmbH & Co. KG, Düren, Germany, thickness 45 μm), and lithium foil (Sigma Aldrich, Schnelldorf, Germany) as the counter electrode. Electrochemical measurements were conducted on a multichannel battery interface (Atlas 0961, Atlas-Sollich, Rębiechowo, Poland) and/or on the Biologic Potentiostat SP200 (BioLogic Science Instruments, Seyssinet-Pariset, France). The samples were measured after a waiting time of ~20 h. The galvanostatic charge–discharge cycles were performed using the constant current–constant voltage protocol (CCCV) in the potential range of 0.005 V–1.5 V with a 15 min potential hold after the lithiation step. Cyclic voltammetry (CV) measurements were conducted with a scan rate of 0.1 mV s^{-1} within the same potential range.

3. Results and Discussion

The carbon phase in SiOC significantly influences their properties as matrices for alloying nanoparticles [11] as well as their electrochemical performance. As we described in our recent work [35], not only is the amount of carbon important but also its structure. We showed that the incorporation of the ordered carbon phase in the form of small graphitic flakes in the SiOC structure is beneficial for electrochemical activity towards lithium ions and cycling stability.

A thorough analysis of SiOC/Sn and SiOC/C/Sn composites by means of Raman spectroscopy helps to correlate the carbon structure with the composites' properties.

The Raman spectra of all investigated materials (Figure 1a) exhibited D and G modes at ~1340 cm^{-1} and ~1580 cm^{-1}, respectively, characteristic of carbonaceous materials. For further analysis, these modes were deconvoluted into five peaks [42], as presented in Figure 1b–f, Figure S1, and Table S1 and Table S2 (in the Supplementary Materials). Pure SiOC exhibits a typical response with a strong D1 peak (I_{D1} = 0.950), related to the disordered forms of carbon, and about half-size G and D2 peak intensities (I_G = 0.441 and I_{D2} = 0.379), corresponding to the ideal and damaged graphitic lattice, respectively [42,43]. The addition of the tin precursor to SiOC (SiOC/Sn-40% sample) led to minor changes in the carbon structure compared to pure SiOC—slightly less intense D1 and D2 bands. On the other hand, replacing part of the ceramic with graphite (in the case of ternary SiOC/C/Sn composites) caused a significant rise in the G band intensity, which is an expected effect for the introduction of ordered carbon networks in the material. An interesting effect is noted when one compares samples with the same amount of graphite but of different tin content. The SiOC:C$_{0.2}$/Sn-60% sample exhibits a lower I_{D1}/I_G ratio than the SiOC:C$_{0.2}$/Sn-40% sample (0.481 vs. 0.551, respectively), suggesting a higher fraction of ordered carbon in sample SiOC:C$_{0.2}$/Sn-40%. This indicates that tin oxide consumes mainly the disordered free carbon phase during the carbothermal reduction process.
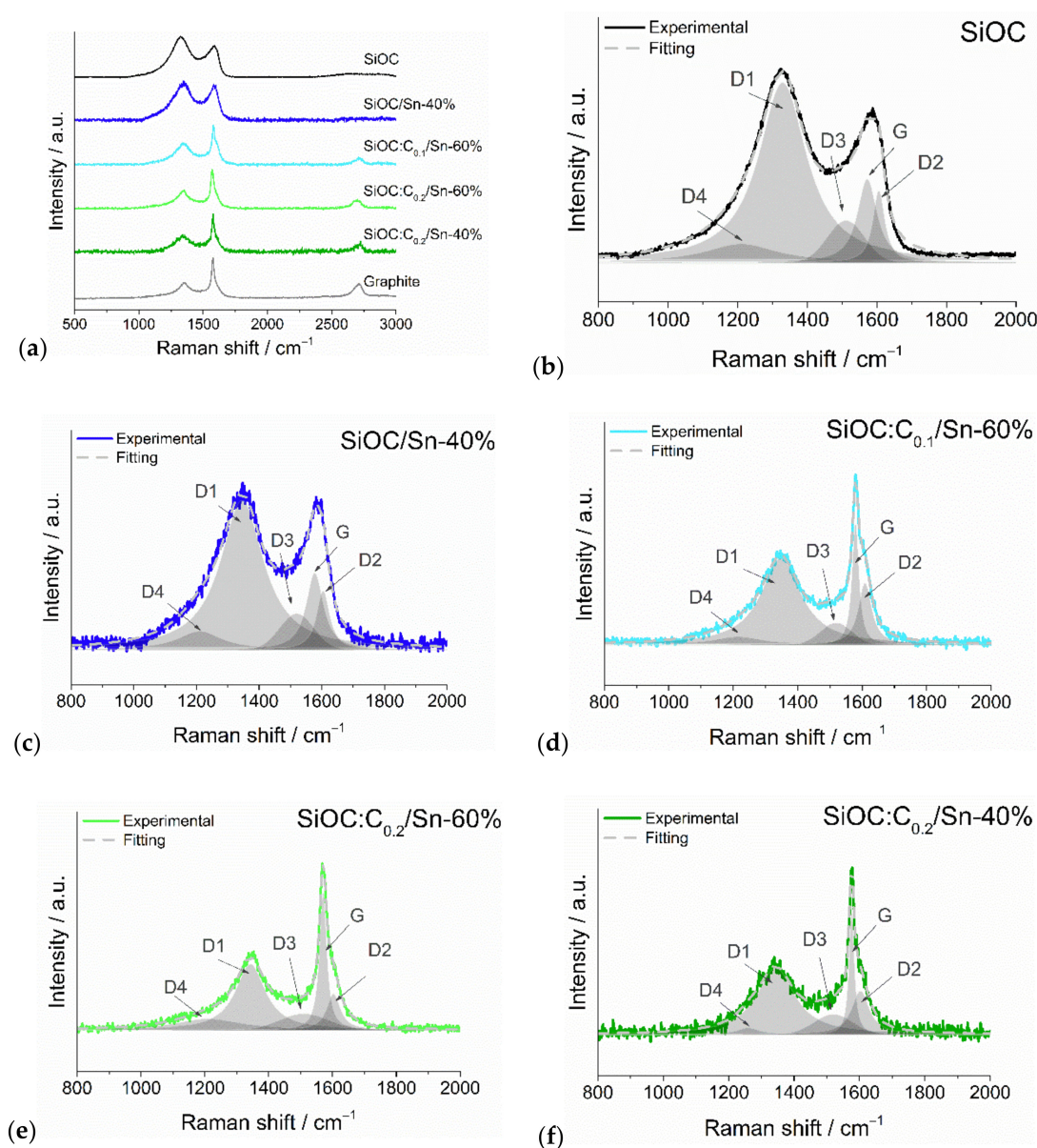
Figure 1. (**a**) Raman spectra of SiOC, graphite and composite materials after background subtraction with custom settings, fitting results for (**b**) pure SiOC, (**c**) SiOC/Sn-40%, (**d**) SiOC:$C_{0.1}$/Sn-60%, (**e**) SiOC:$C_{0.2}$/Sn-60%, and (**f**) SiOC:$C_{0.2}$/Sn-40%.

The structure was further investigated by means of XRD analysis (Figure 2). Pure SiOC (Figure 2 black curve) displayed only a noisy signal with a halo at ~22^0, which is typical for these types of amorphous materials [44]. All ternary composites exhibited a series of sharp peaks coming from graphite and tin. The peaks at 26.2° and 55° confirm the presence of a hexagonal structure of graphite within the composite materials. Other graphitic peaks are missing, probably because of hindrance by the ceramic phase. The remaining peaks of ternary composites correspond to β-tin (the PDF card Sn-ref_00-004-0673 is presented in Table S4 in Supplementary Materials). No signals related to SnO_2 were observed, suggesting complete carbothermal reduction of SnO_2 during pyrolysis. The relative intensities between graphitic and β-Sn depend on the composition, with the graphitic peak more pronounced for the graphite-rich SiOC:$C_{0.2}$/Sn-40% sample and the β-Sn peaks the most intense for the SiOC:$C_{0.1}$/Sn-60% material.
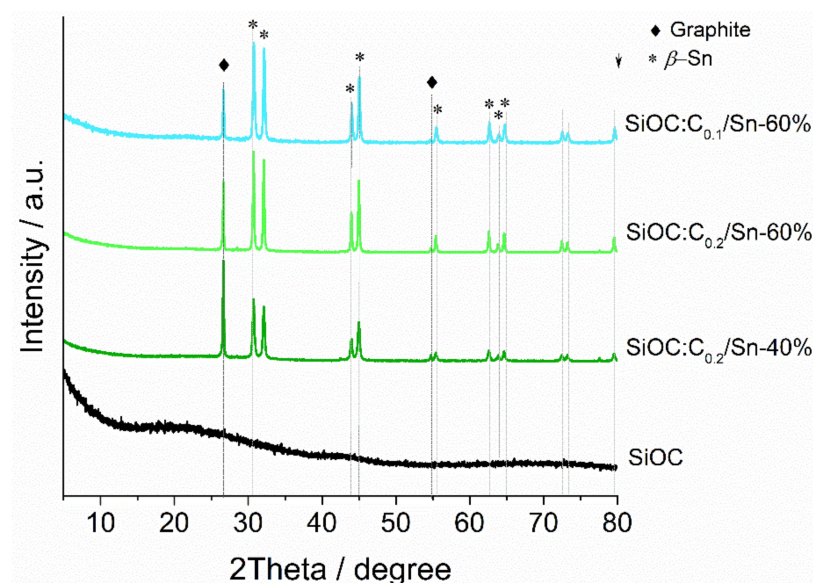
Figure 2. Diffractograms of SiOC and ternary composite materials.

The investigations of morphology, structure, and composition were conducted using SEM-EDX techniques. Figure 3a,b show the morphology of SiOC and SiOC:$C_{0.2}$/Sn-40%, respectively. The pure SiOC powder consisted exclusively of slate rock-like particles of various sizes and shapes. By contrast, tin-containing composites exhibited a large fraction of the crumble-like particles of a coarse texture with plenty of white precipitants and numerous cavities and darker regions with sizes of several microns marked by red circles in Figure 3b (more SEM images for deeper insight are presented in Figures S2 and S3 in Supplementary Materials). The EDX elemental maps (Figure 3c–e) show two distinctive regions: the zones composed mainly of carbon, which can be assigned to the graphite flakes, and the remaining part containing silicon, oxygen, carbon, and tin, which corresponds to the ceramic part. One may notice that the tin nanoparticles are accumulated exclusively in the ceramic part, where a low signal coming from carbon is observed. This result suggests that the free carbon phase from the ceramic part is preferably consumed during the carbothermal reduction process, which is also reflected in the Raman spectra analysis. Such behaviour may be explained by a better mixing of the tin source with the preceramic precursor than with graphite (liquid–liquid in contrast to liquid–solid mixing) as well as a very high activation energy for the carbothermal reduction of tin with graphite [45,46]. This assumption is further supported by the unique morphology of the ceramic region with the cavities and pores coming from the release of CO_2 during the carbothermal reduction. Pure SiOC ceramic is a dense material (specific surface area (SSA) of 3.18 m^2 g^{-1}), whereas the SiOC/Sn-40% composite exhibits SSA of 118.1 m^2 g^{-1} (results of BET analysis are shown in Table S3 and Figure S4 in Supplementary Materials). In the case of the composite materials, the SSA of ternary composites is smaller than that of the binary composite because of the lower ceramic content, which here is partially replaced by graphite. Moreover, comparing the SSA of the composites with the same amount of ceramic and graphite but different tin contents, one may observe higher SSA for SiOC:$C_{0.2}$/Sn-40% (106.9 m^2 g^{-1}) than for SiOC:$C_{0.2}$/Sn-60% (55.1 m^2 g^{-1}). This may result from the more intensive carbothermal reduction process in the ceramic phase, in which the release of CO_2 creates and enlarges porosity, and then the enlarged pores may collapse, leading to the decreased SSA. Furthermore, the SiOC:$C_{0.1}$/Sn-60% composite exhibits a higher SSA (94.6 m^2 g^{-1}) than SiOC:$C_{0.2}$/Sn-60% because of the higher ceramic content and thus a less intensive CO_2 release during the carbothermal reduction. These results further support the hypothesis that graphite does not take part in the carbothermal reduction process.
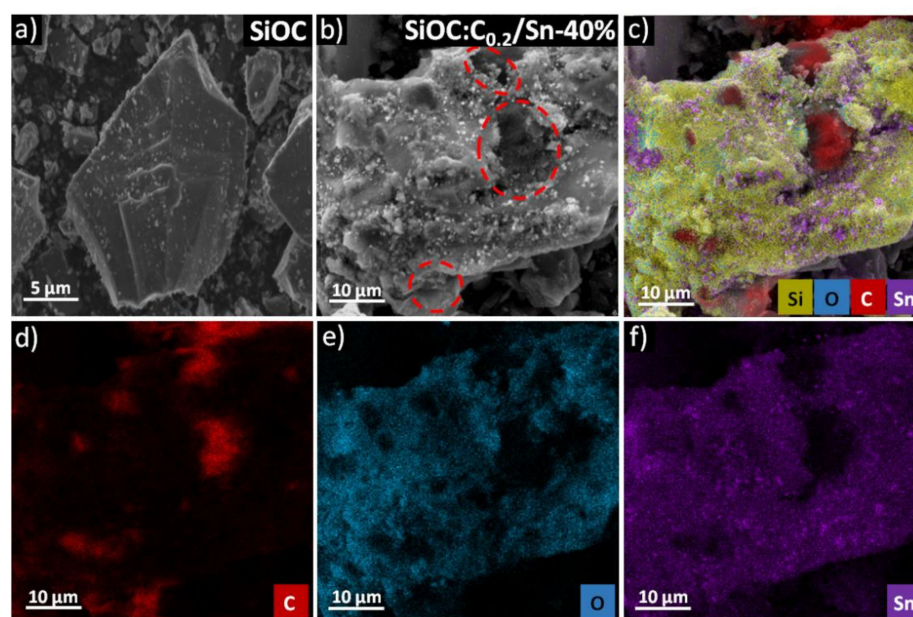
Figure 3. SEM image of (**a**) SiOC and (**b**) SiOC:$C_{0.2}$/Sn-40% composite; (**c–f**) X-ray elemental maps of silicon, carbon, oxygen, and tin of the SiOC:$C_{0.2}$/Sn-40% composite.

A deeper insight into the microstructure of the ternary composites was provided by transmission electron microscopy. TEM images of the binary SiOC/Sn-40% and the ternary SiOC:$C_{0.2}$/Sn-60% composite are shown in Figure 4a,b, respectively. The microstructure of SiOC/Sn-40% consists of tin nanoparticles, represented by black dots, immersed in a featureless amorphous structure of SiOC [47,48]. In comparison, the SiOC:$C_{0.2}$/Sn-60% composite reveals additional parallel smudges typical for graphite [49], which interpenetrate the ceramic component. In both samples, tin nanoparticles are uniformly distributed within the ceramic part. The average size of tin nanoparticles seems to depend on the amount of the ceramic part in the composite, as presented in Figure S5 in the Supplementary Materials. Figure 5a presents the HAADF image of the ternary SiOC:$C_{0.2}$/Sn-60% composite with clearly separated ceramic and graphitic phases. This image confirms that the tin nanoparticles accumulate mainly in the ceramic part (Figure 5b), while in the graphitic phase, there are only a few randomly distributed tin nanoparticles (Figure 5c). The EDX elemental compositions of the selected regions of Figure 5a) are presented in Figure S6 in the Supplementary Materials. The differences between the ternary composites of various tin content are presented in Figure S7 in the Supplementary Materials. It is shown that the samples with a lower content of the tin precursor show much smaller tin accumulation and greater distances between each tin nanoparticle than samples where 60 wt.% of tin precursor was added. These results confirm that carbothermal reduction occurs mainly in the ceramic phase.
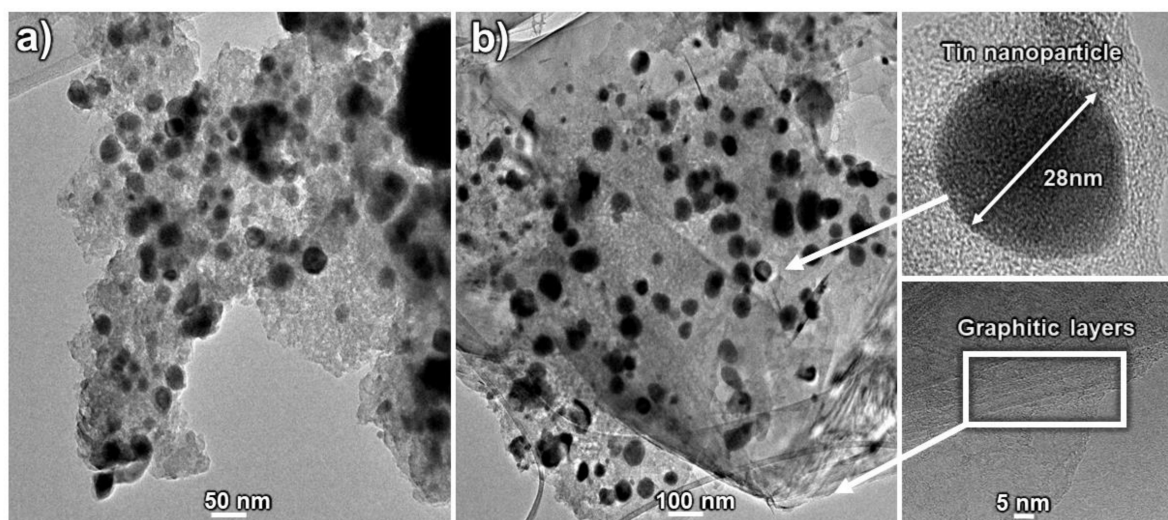
Figure 4. TEM pictures of (**a**) SiOC/Sn-40% and (**b**) SiOC:C$_{0.2}$/Sn-60% composites.
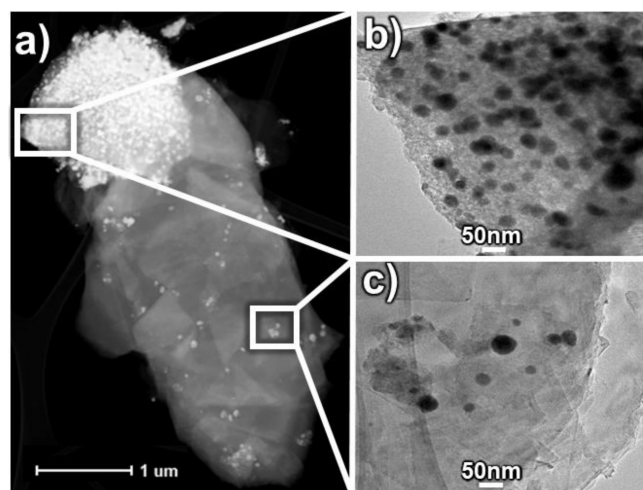

Figure 5. (**a**) HAADF image of a SiOC:C$_{0.2}$/Sn-60% particle with separated ceramic and graphitic phases; TEM images of (**b**) ceramic phase and (**c**) graphitic phase.

The influence of the carbothermal reduction on the ceramic microstructure was tracked through the ^{29}Si solid-state NMR measurements. The pure ceramic sample (Figure 6a) exhibited peaks corresponding to various SiO$_x$C$_y$ mixed bonds tetrahedra, with plenty of Si–C bonds present [50]. On the other hand, all the ternary SiOC/C/Sn composites (Figure 6b–d)) revealed only one peak at around −114 ppm, which corresponds to SiO$_4$ units [51,52]. No peaks indicating Si–C bonds were detected. The presence of exclusively SiO$_4$ units indicates the depletion of carbon atoms bound to Si, which was explained by oxidation of C and Si by SnO$_2$ during its reduction to metallic Sn [14]. These results suggest that during carbothermal reduction, not only the free carbon phase but also carbon from the mixed bonds of silicon tetrahedra are preferably consumed compared with graphite.
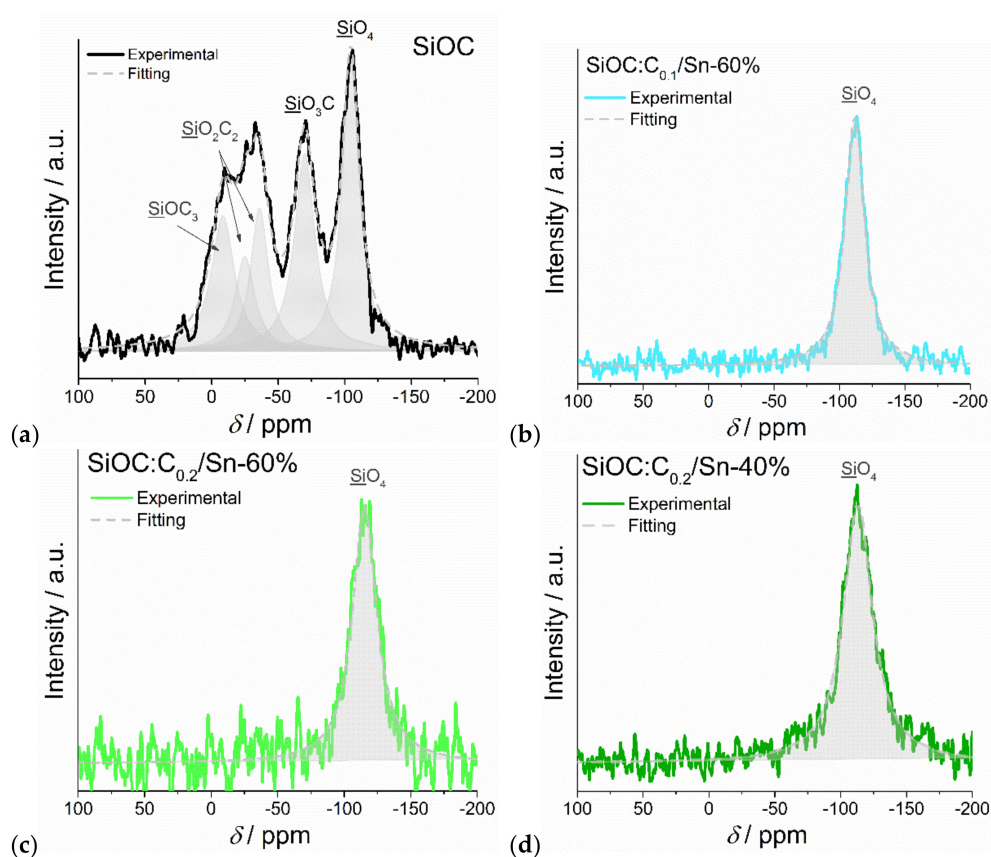
Figure 6. ^{29}Si NMR spectra for (**a**) SiOC (**b**) SiOC:$C_{0.1}$/Sn-60%, (**c**) SiOC:$C_{0.2}$/Sn-60% and (**d**) SiOC:$C_{0.2}$/Sn-40%.

The electrochemical activity of the composite materials was investigated by means of cycling voltammetry and galvanostatic charge–discharge techniques. The CV curves present a general electrochemical pattern similar for all the investigated ternary composites, as presented in Figure 7a,b and Figure S8 in Supplementary Materials. The first cathodic sweep differs from the following cycles. In the first lithiation process, a long shoulder between 1.4 V and 0.66 V emerges, disappearing in subsequent cycles, which can be attributed to the creation of a solid-electrolyte interface (SEI) on all of the three components of the composites [19,53–55]. Then, at lower potentials, a broad feature at about 0.46 V appears, which is related to the formation of different Li_xSn_y alloys, mainly LiSn. In the following cycles, this peak splits into two peaks with maxima at 0.32 V and 0.61 V, which correspond to Li_7Sn_2 and Li_2Sn_5 phases, respectively [55–57]. In the potential range between 0.36 V and 0.005 V, multiple reactions occur, which can be attributed to the creation of high-lithium tin alloys and Li^+ intercalation into the graphite and ceramic phases [53,58–60]. During the anodic sweep at low potentials, three peaks at 0.1, 0.17, and 0.24 V appear, which come from a gradual deinsertion of lithium ions from graphite [53,59]. The following peaks in the range between 0.3 and 0.9 V correspond to a gradual dealloying of Li_xSn_y [57]. A small broad peak at approximately 1.1 V, fading with the following cycles, can be attributed to partial oxidation of ~1 nm size Sn nanoparticles [61,62]. The cyclic voltammetry curves confirm the electrochemical activity of all components of the composites and indicate the creation of both high intercalation graphite stages (LiC_6) and high-lithium tin compounds. The electrochemical activity of the ternary composites of different compositions is compared in Figure 7b. The activity of graphite is the lowest for the SiOC:$C_{0.1}$/Sn-60% sample, which is a direct consequence of having the lowest graphite content among all the samples. In addition, the tin alloying currents are the smallest for the sample with the lowest tin content, namely SiOC:$C_{0.2}$/Sn-40%. These results suggest that

the electrochemical response of each component is related to the amount of that component in the composite material.
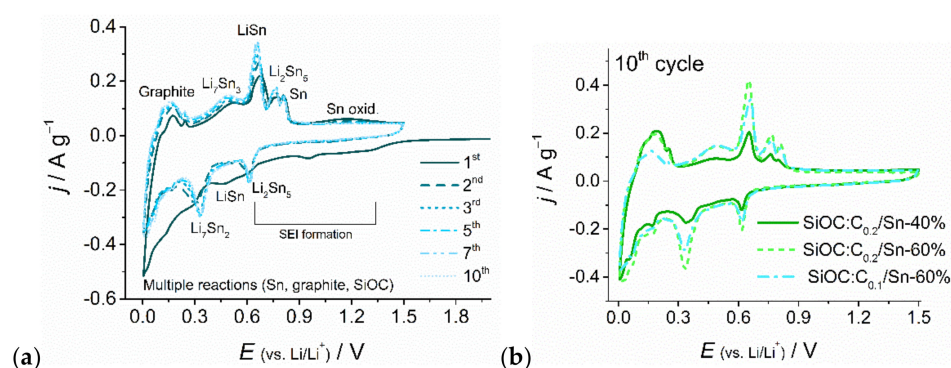

Figure 7. (**a**) Cyclic voltammetry measurements of selected cycles of $SiOC:C_{0.1}/Sn$-60% composite, and (**b**) comparison of the 10th cycle of the ternary composites.

Figure 8 presents voltage profiles for the first and second cycles for ternary composite materials in the 0.005–1.5 V potential range. In the first lithiation process, there are no distinct plateaux, which corresponds well to the first cathodic polarization on the CV curves (Figure 7a and Figure S8 in Supplementary Materials), where no distinct redox peaks are observed. In the second and the following cycles, multiple plateaux are observed, indicating the creation of Sn_xLi_y alloys and stepwise Li^+ intercalation into graphite. During delithiation steps the redox activities of graphite (Figure 8a inset) and tin (Figure 8b) towards lithium ions are clearly depicted. The sloping shape of charge–discharge curves is typical for the ceramic component. The results confirm the electrochemical activity of all the composite components. The initial lithiation capacity for obtained materials varies between 1000–1300 mAh g^{-1}, and it drops by approximately half of the value over the first few cycles. The first delithiation capacity equals 439, 507, and 515 mAh g^{-1} for the $SiOC:C_{0.2}/Sn$-40%, $SiOC:C_{0.2}/Sn$-60%, and $SiOC:C_{0.1}/Sn$-60% samples respectively, which gives first cycle efficiency of around 45% in the 0.005 V–1.5 V potential range (57–63% in the 0.005 V–3 V potential range), as presented in Table 2. Such high capacity loss during the first cycle is mostly related to the creation of complex SEI graphite, tin, and ceramic phases and to irreversible lithium bonding with the ceramic phase [16,63]. The SEI creation process is additionally enhanced by a high specific surface area, which increases the contact between the active material and electrolyte and thus promotes higher lithium-ion consumption [64].
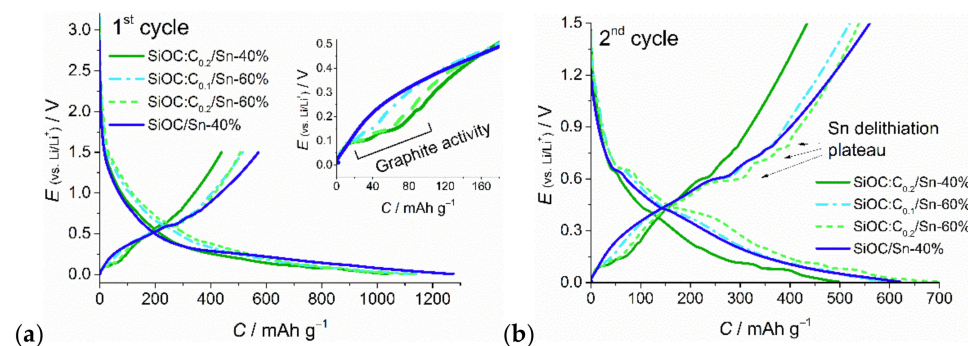

Figure 8. Voltage profiles of the ternary composites: (**a**) 1st cycle, (**b**) 2nd cycle.

Table 2. Selected electrochemical results. Coulombic efficiencies η within 0.005 V–1.5 V and 0.005 V–3 V potential regions were calculated by dividing the first lithiation capacity by the first delithiation capacity obtained in certain potential regions.

Material	1st Cycle C_{irrev}/mAh g^{-1}	1st Cycle C_{rev}/mAh g^{-1}	η (0.005 V–1.5 V)/%	η (0.005 V–3 V) /%
SiOC:C$_{0.2}$/Sn-40%	600	439	42	56.5
SiOC:C$_{0.2}$/Sn-60%	623	507	45	62
SiOC:C$_{0.1}$/Sn-60%	625	515	45	63
SiOC/Sn-40%	699	572	45	65

Figure 9a presents cyclic stability measurements of ternary composites within the 0.005 V–3 V potential range. After the initial cycles, the capacity of tin-rich samples, i.e., SiOC:C$_{0.2}$/Sn-60% and SiOC:C$_{0.1}$/Sn-60%, is around 610 mAh g^{-1}, while the capacity of SiOC:C$_{0.2}$/Sn-40% stays around 480 mAh g^{-1}. This indicates that the tin nanoparticles are the major lithium storage sites within composites, and increasing tin content indeed leads to a higher capacity. In subsequent cycles, the capacity of SiOC:C$_{0.1}$/Sn-60% gradually fades, while for other materials, it remains rather stable. Fast capacity fading for SiOC/Sn composites was previously reported as the result of insufficient carbon content within the material due to the carbothermal reduction process [12]. This problem is more pronounced in the composites in which the tin precursor was used in quantities higher than 40 wt.% with regard to a mass reaction mixture [13]. In the case of the SiOC:C$_{0.1}$/Sn-60% composite, the stability over 100 cycles is much worse than that for the SiOC:C$_{0.2}$/Sn-60% (52.7 vs. 86.5%). The results show that graphite, although not protecting the free carbon phase from the consumption in the carbothermal reduction process, can in an appropriate amount provide the required softness and electrical conductivity for good stability over extended cycling. SEM images of the electrode layers before and after cycling are presented in Figure S9 (in Supplementary Materials). The morphology of the electrode layers of the composites with a lower number of tin nanoparticles (SiOC/Sn-40% and SiOC:C$_{0.2}$/Sn-40%) does not change after extended cycling tests (Figure S9a,b), whereas the SiOC:C$_{0.2}$/Sn-60%) exhibit some cracks (Figure S9c, which may be attributed to the higher Sn concentration and associated volume changes upon alloying as the tin nanoparticles are accumulated mainly on the ceramic part.
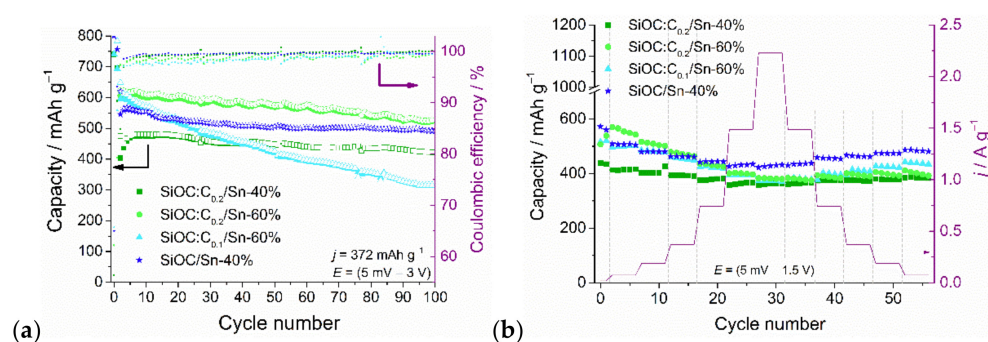

Figure 9. (**a**) Cycling stability at 372 mA g^{-1} and the corresponding Coulombic efficiencies; (**b**) rate capability of the ternary SiOC/C/Sn composites.

The XRD analysis of cycled samples are presented in Figure S10 (in Supplementary Materials). The diffractograms are quite complex and reveal the presence of graphite, β-Sn (components of the composites), Li$_2$CO$_3$, Sn$_3$O$_4$ (components typical for SEI on tin containing electrodes) [65–67], Li$_2$Sn$_5$ (one of the lowest lithiation states of Li-Sn alloys), and Cu (current collector). The XRD patterns of the cycled binary and ternary composites are similar. A quantitative analysis would be ambiguous because of the overlapping of the XRD reflexes and strong peaks coming from the copper current collector.

To give some overview, we compared our ternary composites to the state-of-the-art SiOC/Sn-40%, which was reported as the best performing SiOC/Sn composite [13]. The capacity of SiOC/Sn-40% is around 520 mAh g^{-1} with a stability of 90.1% over 100 cycles. It appears that the capacity of SiOC/Sn-40% is lower than the capacity of the SiOC:C$_{0.2}$/Sn-60% sample but higher than that of SiOC:C$_{0.2}$/Sn-40%, while the stability is similar to the stability of these samples. These results indicate that the capacity strongly depends on the composition in a way that the presence of tin increases the capacity of composites, while graphite decreases it, which can be expected taking into account their theoretical capacity values. However, graphite can be a good component improving the ability of the host matrix to host higher tin content, which in turn can help increase the overall capacity of a ternary composite compared to the binary one.

The rate capability measurements within the 5 mV–1.5 V potential range are presented in Figure 9b. At lower current rates (C/5 and C/2 in respect to graphite) the SiOC:C$_{0.2}$/Sn-60% composite exhibits the highest capacity values. However, with increasing polarization currents (above 1C–372 mA g^{-1}) capacity values of all the ternary composites decrease more rapidly than for the binary SiOC/Sn-40% composite. Moreover, after returning to the low polarization currents, the capacities of the ternary composite do not increase as in the case of the binary composite. These results show that the composites with graphite are sensitive to high currents. The pure graphitic electrode also exhibits capacity fading at currents higher than 1C due to uneven SEI formation and lithium plating [68,69]. On the other hand, SiOC ceramics are known as stable materials at high current rates [24,70,71].

4. Conclusions

In this work, we reported a novel silicon oxycarbide–graphite–tin nanoparticle composite for lithium-ion batteries. Samples were produced using flake graphite and liquid preceramic and tin precursors via an ultrasound–enhanced hydrosilylation reaction. Employing high power probe sonication ensures the homogeneous mixing of all components and accelerates the cross-linking process. Final ternary composites were obtained through pyrolysis, which transformed the preceramic polymer into carbon-rich silicon oxycarbide and tin precursor into the tin nanoparticles via carbothermal reduction. This resulted in homogeneous composites with tin nanoparticles uniformly distributed mainly in the ceramic phase.

We observed that during carbothermal reduction of the tin precursor, carbon coming from the free carbon phase and mixed bonds silicon tetrahedra is preferably consumed over graphite. This is related to better mixing of the tin precursor with the preceramic polymer, as well as the high activation energy for the SnO$_2$–graphite reaction. In our system, graphite provided appropriate conductivity and softness for stable alloying–dealloying of tin nanoparticles upon multiple cycles and also actively intercalated/deintercalated lithium ions. Replacing part of the ceramic matrix with graphite enabled an increase in the tin content with regard to literature reports, without deteriorating electrochemical stability upon prolonged charge-discharge cycles. Our best performing sample, SiOC:C$_{0.2}$/Sn-60%, delivers a capacity about 100 mAh g^{-1} higher than the state-of-the-art SiOC/Sn-40% measured at the same conditions, while the stability at 1C was roughly the same. However, ternary composites are sensitive to high polarization currents (above 1C) because of the graphitic component.

nanoparticles in the SiOC:C/Sn and SiOC/Sn nanocomposites. $SiOC_{Pre}$ content corresponds to the weight percentage content of preceramic polymer in preceramic blend.; Figure S6. EDX elemental composition of tin-rich (SiOC) and tin-poor (graphite) regions of the $SiOC:C_{0.2}$/Sn-60% sample.; Figure S7. SEM images of (a) $SiOC:C_{0.2}$/Sn-40% and (b) $SiOC:C_{0.1}$/Sn-60% composites showing accumulation of tin nanoparticles in the ceramic phase.; Figure S8. Cyclic voltammetry curves of (a) $SiOC:C_{0.2}$/Sn-60%, (b) $SiOC:C_{0.1}$/Sn-60% and c) $SiOC:C_{0.2}$/Sn-40%.; Figure S9. SEM images of electrode layers before ("fresh") and after extended cycling tests (2 cycles at 18.6 mA g^{-1} followed by 100 cycles at 372 mA g^{-1}) recorded for a) SiOC/Sn-40%, (b) $SiOC:C_{0.2}$/Sn-40% and (c) $SiOC:C_{0.2}$/Sn-60%.; Figure S10. Diffractograms of the cycled electrodes, Inset: the selected 2Theta range of the diffractogram of $SiOC:C_{0.2}$/Sn-60% composite.

Author Contributions: D.K.: Investigation, Formal Analysis, Data Curation, Visualization, Writing—Original Draft, Writing—Review and Editing; P.V.W.S.: Conceptualization, Methodology, Investigation, Writing—Original Draft, Supervision, Funding Acquisition, Writing—Review and Editing; P.M.: Formal analysis, Visualization; G.B.: Writing—Original Draft, Funding Acquisition, Writing—Review and Editing; M.G.: Formal Analysis; N.K.: Formal Analysis; M.W.-Z.: Conceptualization, Formal Analysis, Visualization, Supervision, Writing—Original Draft, Funding Acquisition, Writing—Review and Editing. All authors have read and agreed to the published version of the manuscript.

Data Availability Statement: The data presented in this study are available on request from the corresponding author.

Conflicts of Interest: The authors declare no conflict of interest.

References

1. Obrovac, M.N.; Chevrier, V.L. Alloy Negative Electrodes for Li-Ion Batteries. *Chem. Rev.* **2014**, *114*, 11444–11502. [CrossRef] [PubMed]
2. Scrosati, B.; Hassoun, J.; Sun, Y.-K. Lithium-ion batteries. A look into the future. *Energy Environ. Sci.* **2011**, *4*, 3287–3295. [CrossRef]
3. Zhang, M.; Wang, T.; Cao, G. Promises and challenges of tin-based compounds as anode materials for lithium-ion batteries. *Int. Mater. Rev.* **2015**, *60*, 330–352. [CrossRef]
4. Xu, Y.; Liu, Q.; Zhu, Y.; Liu, Y.; Langrock, A.; Zachariah, M.R.; Wang, C. Uniform nano-Sn/C composite anodes for lithium ion batteries. *Nano Lett.* **2013**, *13*, 470–474. [CrossRef] [PubMed]
5. Wang, Y.; Lee, J.Y.; Deivaraj, T.C. Tin Nanoparticle Loaded Graphite Anodes for Li-Ion Battery Applications. *J. Electrochem. Soc.* **2004**, *151*, A1804. [CrossRef]
6. Idota, Y.; Kubota, T.; Matsufuji, A. Tin-Based Amorphous Oxide: A High-Capacity Lithium-Ion—Storage Material. *Science* **1997**, *31*, 1395–1398. [CrossRef]
7. Mao, O.; Dahn, J.R. Mechanically Alloyed Sn-Fe(-C) Powders as Anode Materials for Li-Ion Batteries: II. The Sn-Fe System. *J. Electrochem. Soc.* **1999**, *146*, 405–413. [CrossRef]
8. Tamura, N.; Ohshita, R.; Fujimoto, M.; Fujitani, S.; Kamino, M.; Yonezu, I. Study on the anode behavior of Sn and Sn-Cu alloy thin-film electrodes. *J. Power Sources* **2002**, *107*, 48–55. [CrossRef]
9. Kamali, A.R.; Fray, D.J. Tin-based materials as advanced anode materials for lithium ion batteries: A review. *Rev. Adv. Mater. Sci.* **2011**, *27*, 14–24.
10. Derrien, G.; Hassoun, J.; Panero, S.; Scrosati, B. Nanostructured Sn-C composite as an advanced anode material in high-performance lithium-ion batteries. *Adv. Mater.* **2007**, *19*, 2336–2340. [CrossRef]
11. Rohrer, J.; Vrankovic, D.; Cupid, D.; Riedel, R.; Seifert, H.J.; Albe, K.; Graczyk-Zajac, M. Si-and Sn-containing SiOCN-based nanocomposites as anode materials for lithium ion batteries: Synthesis, thermodynamic characterization and modeling. *Int. J. Mater. Res.* **2017**, *108*, 920–932. [CrossRef]
12. Kaspar, J.; Terzioglu, C.; Ionescu, E.; Graczyk-Zajac, M.; Hapis, S.; Kleebe, H.J.; Riedel, R. Stable SiOC/Sn nanocomposite anodes for lithium-ion batteries with outstanding cycling stability. *Adv. Funct. Mater.* **2014**, *24*, 4097–4104. [CrossRef]

13. Dubey, R.J.-C.; Sasikumar, P.V.W.; Krumeich, F.; Blugan, G.; Kuebler, J.; Kravchyk, K.V.; Graule, T.; Kovalenko, M.V. Silicon Oxycarbide—Tin Nanocomposite as a High-Power-Density Anode for Li-Ion Batteries. *Adv. Sci.* **2019**, *6*, 1901220. [CrossRef] [PubMed]

14. Tolosa, A.; Widmaier, M.; Krüner, B.; Griffin, J.M.; Presser, V. Continuous silicon oxycarbide fiber mats with tin nanoparticles as a high capacity anode for lithium-ion batteries. *Sustain. Energy Fuels* **2018**, *2*, 215–228. [CrossRef]

15. Kaspar, J.; Graczyk-Zajac, M.; Choudhury, S.; Riedel, R. Impact of the electrical conductivity on the lithium capacity of polymer-derived silicon oxycarbide (SiOC) ceramics. *Electrochim. Acta* **2016**, *216*, 196–202. [CrossRef]

16. Graczyk-Zajac, M.; Reinold, L.M.; Kaspar, J.; Sasikumar, P.V.W.; Soraru, G.D.; Riedel, R. New insights into understanding irreversible and reversible lithium storage within SIOC and SICN ceramics. *Nanomaterials* **2015**, *5*, 233–245. [CrossRef]

17. Colombo, P.; Mera, G.; Riedel, R.; Sorarù, G.D. Polymer-derived ceramics: 40 Years of research and innovation in advanced ceramics. *J. Am. Ceram. Soc.* **2010**, *93*, 1805–1837. [CrossRef]

18. Erb, D.; Lu, K. Additive and pyrolysis atmosphere effects on polysiloxane-derived porous SiOC ceramics. *J. Eur. Ceram. Soc.* **2017**, *37*, 4547–4557. [CrossRef]

19. Xia, K.; Wu, Z.; Xuan, C.; Xiao, W.; Wang, J.; Wang, D. Effect of KOH etching on the structure and electrochemical performance of SiOC anodes for lithium-ion batteries. *Electrochim. Acta* **2017**, *245*, 287–295. [CrossRef]

20. Stabler, C.; Celarie, F.; Rouxel, T.; Limbach, R.; Wondraczek, L.; Riedel, R.; Ionescu, E. Effect of composition and high-temperature annealing on the local deformation behavior of silicon oxycarbides. *J. Eur. Ceram. Soc.* **2019**, *39*, 2287–2296. [CrossRef]

21. Stabler, C.; Reitz, A.; Stein, P.; Albert, B.; Riedel, R.; Ionescu, E. Thermal properties of SiOC glasses and glass ceramics at elevated temperatures. *Materials* **2018**, *11*, 279. [CrossRef] [PubMed]

22. Pradeep, V.S.; Graczyk-Zajac, M.; Wilamowska, M.; Riedel, R.; Soraru, G.D. Influence of pyrolysis atmosphere on the lithium storage properties of carbon-rich polymer derived SiOC ceramic anodes. *Solid State Ionics* **2014**, *262*, 22–24. [CrossRef]

23. Wilamowska, M.; Pradeep, V.S.; Graczyk-Zajac, M.; Riedel, R.; Sorarù, G.D. Tailoring of SiOC composition as a way to better performing anodes for Li-ion batteries. *Solid State Ionics* **2014**, *260*, 94–100. [CrossRef]

24. Wilamowska-Zawlocka, M.; Puczkarski, P.; Grabowska, Z.; Kaspar, J.; Graczyk-Zajac, M.; Riedel, R.; Sorarù, G.D. Silicon oxycarbide ceramics as anodes for lithium ion batteries: Influence of carbon content on lithium storage capacity. *RSC Adv.* **2016**, *6*, 104597–104607. [CrossRef]

25. Kaspar, J.; Graczyk-Zajac, M.; Riedel, R. Carbon-rich SiOC anodes for lithium-ion batteries: Part II. Role of thermal cross-linking. *Solid State Ionics* **2012**, *225*, 527–531. [CrossRef]

26. Cordelair, J.; Greil, P. Electrical conductivity measurements as a microprobe for structure transitions in polysiloxane derived Si-O-C ceramics. *J. Eur. Ceram. Soc.* **2000**, *20*, 1947–1957. [CrossRef]

27. Wilson, A.M.; Xing, W.; Zank, G.; Yates, B.; Dahn, J.R. Pyrolysed pitch-polysilane blends for use as anode materials in lithium ion batteries II: The effect of oxygen. *Solid State Ionics* **1997**, *100*, 259–266. [CrossRef]

28. Larcher, D.; Mudalige, C.; George, A.E.; Porter, V.; Gharghouri, M.; Dahn, J.R. Si-containing disordered carbons prepared by pyrolysis of pitch/polysilane blends: Effect of oxygen and sulfur. *Solid State Ionics* **1999**, *122*, 71–83. [CrossRef]

29. Dibandjo, P.; Graczyk-Zajac, M.; Riedel, R.; Pradeep, V.S.; Soraru, G.D. Lithium insertion into dense and porous carbon-rich polymer-derived SiOC ceramics. *J. Eur. Ceram. Soc.* **2012**, *32*, 2495–2503. [CrossRef]

30. Blum, Y.D.; MacQueen, D.B.; Kleebe, H.J. Synthesis and characterization of carbon-enriched silicon oxycarbides. *J. Eur. Ceram. Soc.* **2005**, *25*, 143–149. [CrossRef]

31. Fukui, H.; Ohsuka, H.; Hino, T.; Kanamura, K. Influence of polystyrene/phenyl substituents in precursors on microstructures of Si-O-C composite anodes for lithium-ion batteries. *J. Power Sources* **2011**, *196*, 371–378. [CrossRef]

32. David, L.; Bhandavat, R.; Barrera, U.; Singh, G. Silicon oxycarbide glass-graphene composite paper electrode for long-cycle lithium-ion batteries. *Nat. Commun.* **2016**, *7*, 10998–11008. [CrossRef] [PubMed]

33. Shao, G.; Hanaor, D.A.H.; Wang, J.; Kober, D.; Li, S.; Wang, X.; Shen, X.; Bekheet, M.F.; Gurlo, A. Polymer derived SiOC integrated with graphene aerogel as highly stable Li-ion battery anodes. *ACS Appl. Mater. Interfaces* **2020**, *12*, 46045–46056. [CrossRef] [PubMed]

34. Bhandavat, R.; Singh, G. Stable and efficient li-ion battery anodes prepared from polymer-derived silicon oxycarbide-carbon nanotube shell/core composites. *J. Phys. Chem. C* **2013**, *117*, 11899–11905. [CrossRef]

35. Knozowski, D.; Graczyk-Zajac, M.; Vrankovic, D.; Trykowski, G.; Sawczak, M.; De Carolis, D.M.; Wilamowska-Zawłocka, M. New insights on lithium storage in silicon oxycarbide/carbon composites: Impact of microstructure on electrochemical properties. *Compos. Part B Eng.* **2021**, 109302. [CrossRef]

36. Konno, H.; Morishita, T.; Sato, S.; Habazaki, H.; Inagaki, M. High-capacity negative electrode materials composed of Si-C-O glass-like compounds and exfoliated graphite for lithium ion battery. *Carbon N. Y.* **2005**, *43*, 1111–1114. [CrossRef]

37. Knozowski, D.; Graczyk-Zajac, M.; Trykowski, G.; Wilamowska-Zawłocka, M. Silicon oxycarbide-graphite electrodes for high-power energy storage devices. *Materials* **2020**, *13*, 4302. [CrossRef]

38. Wu, Z.; Cheng, X.; Tian, D.; Gao, T.; He, W.; Yang, C. SiOC nanolayers directly-embedded in graphite as stable anode for high-rate lithium ion batteries. *Chem. Eng. J.* **2019**, *375*, 121997. [CrossRef]

39. Graczyk-Zajac, M.; Fasel, C.; Riedel, R. Polymer-derived-SiCN ceramic/graphite composite as anode material with enhanced rate capability for lithium ion batteries. *J. Power Sources* **2011**, *196*, 6412–6418. [CrossRef]

40. Veeraraghavan, B.; Durairajan, A.; Haran, B.; Popov, B.; Guidotti, R. Study of Sn-Coated Graphite as Anode Material for Secondary Lithium-Ion Batteries. *J. Electrochem. Soc.* **2002**, *149*, A675. [CrossRef]

41. Nobili, F.; Mancini, M.; Dsoke, S.; Tossici, R.; Marassi, R. Low-temperature behavior of graphite-tin composite anodes for Li-ion batteries. *J. Power Sources* **2010**, *195*, 7090–7097. [CrossRef]

42. Sadezky, A.; Muckenhuber, H.; Grothe, H.; Niessner, R.; Pöschl, U. Raman microspectroscopy of soot and related carbonaceous materials: Spectral analysis and structural information. *Carbon N. Y.* **2005**, *43*, 1731–1742. [CrossRef]

43. Ferrari, A.C.; Robertson, J. Interpretation of Raman spectra of disordered and amorphous carbon. *Phys. Rev. B* **2000**, *61*, 14095–14107. [CrossRef]

44. Sorarù, G.D.; Modena, S.; Guadagnino, E.; Colombo, P.; Egan, J.; Pantano, C. Chemical Durability of Silicon Oxycarbide Glasses. *J. Am. Ceram. Soc.* **2002**, *85*, 1529–1536. [CrossRef]

45. Leveîque, G.; Abanades, S. Thermodynamic and kinetic study of the carbothermal reduction of SnO_2 for solar thermochemical fuel generation. *Energy Fuels* **2014**, *28*, 1396–1405. [CrossRef]

46. Padilla, R.; Sohn, H.Y. The reduction of stannic oxide with carbon. *Metall. Trans. B* **1979**, *10*, 109–115. [CrossRef]

47. Kleebe, H.J.; Blum, Y.D. SiOC ceramic with high excess free carbon. *J. Eur. Ceram. Soc.* **2008**, *28*, 1037–1042. [CrossRef]

48. Swain, I.P.; Sadual, N.; Behera, S.K. Porosity and nanostructure of silicon oxycarbide derived carbon. *Open Ceram.* **2021**, *6*, 100116. [CrossRef]

49. Moumeni, E.; Tiedje, N.S.; Horsewell, A.; Hattel, J.H. A TEM study on the Microstructure of fine flaky graphite. In Proceedings of the 52nd International Foundry Conference, Portoroz, Slovenia, 12–14 September 2012; pp. 1–9.

50. Dubey, R.J.C.; Sasikumar, P.V.W.; Cerboni, N.; Aebli, M.; Krumeich, F.; Blugan, G.; Kravchyk, K.V.; Graule, T.; Kovalenko, M.V. Silicon oxycarbide-antimony nanocomposites for high-performance Li-ion battery anodes. *Nanoscale* **2020**, *12*, 13540–13547. [CrossRef]

51. Widgeon, S.J.; Sen, S.; Mera, G.; Ionescu, E.; Riedel, R.; Navrotsky, A. 29Si and 13C Solid-state NMR spectroscopic study of nanometer-scale structure and mass fractal characteristics of amorphous polymer derived silicon oxycarbide ceramics. *Chem. Mater.* **2010**, *22*, 6221–6228. [CrossRef]

52. Zhang, H.; Patano, C.G. Synthesis and Characterization of Silicon Oxycarbide Glasses. *J. Am. Ceram. Soc.* **1990**, *73*, 958–963. [CrossRef]

53. Seidl, L.; Martens, S.; Ma, J.; Stimming, U.; Schneider, O. In situ scanning tunneling microscopy studies of the SEI formation on graphite electrodes for Li^+-ion batteries. *Nanoscale* **2016**, *8*, 14004–14014. [CrossRef] [PubMed]

54. Zhang, S.; Ding, M.S.; Xu, K.; Allen, J.; Jow, T.R. Understanding solid electrolyte interface film formation on graphite electrodes. *Electrochem. Solid-State Lett.* **2001**, *4*, 206–208. [CrossRef]

55. Yan, Y.; Ben, L.; Zhan, Y.; Huang, X. Nano-Sn embedded in expanded graphite as anode for lithium ion batteries with improved low temperature electrochemical performance. *Electrochim. Acta* **2016**, *187*, 186–192. [CrossRef]

56. Winter, M.; Besenhard, J.O. Electrochemical lithiation of tin and tin-based intermetallics and composites. *Electrochim. Acta* **1999**, *45*, 31–50. [CrossRef]

57. Lorie Lopez, J.L.; Grandinetti, P.J.; Co, A.C. Phase transformations and capacity fade mechanism in LixSn nanoparticle electrodes revealed by operando 7Li NMR. *J. Mater. Chem. A* **2019**, *7*, 10781–10794. [CrossRef]

58. Graczyk-Zajac, M.; Toma, L.; Fasel, C.; Riedel, R. Carbon-rich SiOC anodes for lithium-ion batteries: Part I. Influence of material UV-pre-treatment on high power properties. *Solid State Ionics* **2012**, *225*, 522–526. [CrossRef]

59. Levi, M.D.; Aurbach, D. Simultaneous measurements and modeling of the electrochemical impedance and the cyclic voltammetric characteristics of graphite electrodes doped with lithium. *J. Phys. Chem. B* **1997**, *101*, 4630–4640. [CrossRef]

60. Smrekar, S.; Bracamonte, M.V.; Primo, E.N.; Luque, G.L.; Thomas, J.; Barraco, D.E.; Leiva, E. A Mapping of the Physical and Electrochemical Properties of Composite Lithium-Ion Batteries Anodes Made from Graphite, Sn, and Si. *Batter. Supercaps* **2020**, *3*, 1248–1256. [CrossRef]

61. Böhme, S.; Edström, K.; Nyholm, L. On the electrochemistry of tin oxide coated tin electrodes in lithium-ion batteries. *Electrochim. Acta* **2015**, *179*, 482–494. [CrossRef]

62. Dufficy, M.K.; Huang, S.Y.; Khan, S.A.; Fedkiw, P.S. Effects of composition and structure on the performance of tin/graphene-containing carbon nanofibers for Li-ion anodes. *RSC Adv.* **2017**, *7*, 15428–15438. [CrossRef]

63. Kroll, P. Tracing Reversible and Irreversible Li Insertion in SiCO Ceramics with Modeling and Ab-Initio Simulations. *MRS Proc.* **2011**, *1313*, 70701–70706. [CrossRef]

64. Ruggeri, I.; Martin, J.; Wohlfahrt-Mehrens, M.; Mancini, M. Interfacial kinetics and low-temperature behavior of spheroidized natural graphite particles as anode for Li-ion batteries. *J. Solid State Electrochem.* **2022**, *26*, 73–83. [CrossRef]

65. Lucas, I.T.; Pollak, E.; Kostecki, R. In situ AFM studies of SEI formation at a Sn electrode. *Electrochem. commun.* **2009**, *11*, 2157–2160. [CrossRef]

66. Wagner, M.R.; Raimann, P.R.; Trifonova, A.; Moeller, K.C.; Besenhard, J.O.; Winter, M. Electrolyte decomposition reactions on tin-And graphite-based anodes are different. *Electrochem. Solid-State Lett.* **2004**, *7*, 2–7. [CrossRef]

67. Eom, K.S.; Jung, J.; Lee, J.T.; Lair, V.; Joshi, T.; Lee, S.W.; Lin, Z.; Fuller, T.F. Improved stability of nano-Sn electrode with high-quality nano-SEI formation for lithium ion battery. *Nano Energy* **2015**, *12*, 314–321. [CrossRef]

68. Li, N.; Sun, M.Z.; Hwang, S.; Li, S.; Zhao, H.Y.; Du, Y.P.; Huang, B.L.; Su, D. Non-equilibrium insertion of lithium ions into graphite. *J. Mater. Chem. A* **2021**, *9*, 12080–12086. [CrossRef]

69. Zhang, P.; Yuan, T.; Pang, Y.; Peng, C.; Yang, J.; Ma, Z.-F.; Zheng, S. Influence of Current Density on Graphite Anode Failure in Lithium-Ion Batteries. *J. Electrochem. Soc.* **2019**, *166*, A5489–A5495. [CrossRef]

70. Sasikumar, P.V.W.; Zera, E.; Graczyk-Zajac, M.; Riedel, R.; Soraru, G.D. Structural Design of Polymer-Derived SiOC Ceramic Aerogels for High-Rate Li Ion Storage Applications. *J. Am. Ceram. Soc.* **2016**, *99*, 2977–2983. [CrossRef]

71. Pradeep, V.; Ayana, D.G.; Graczyk-Zajac, M.; Soraru, G.; Riedel, R. High Rate Capability of SiOC Ceramic Aerogels with Tailored Porosity as Anode Materials for Li-ion Batteries. *Electrochim. Acta.* **2015**, *157*, 41–45. [CrossRef]

72. Swanson , H.E.; Tatge, E. Data for 54 inorganic substances. *NBS Circ.* **1953**, *539*, 24.